Monte Carlo method with SNBCK nongray gas model for thermal radiation in containment flows

Xiongguo Liu[a], Stephan Kelm[a,*], Manohar Kampili[a], Vijaya Kumar G.[a,b], Hans-Josef Allelein[a]

[a] *Forschungszentrum Jülich GmbH, Institute of Energy and Climate Research (IEK-6), Jülich, Germany*
[b] *Indian Institute of Technology Madras, Department of Applied Mechanics, Chennai, India*

Abstract

During a postulated severe accident in light water reactors, containment flows are characterized by relatively low velocities and modest temperature differences after depressurization of the reactor cooling system. Owing to the low gas temperature level and small temperature differences, gas radiation heat transfer was neglected in CFD simulations of hydrogen transport and mixing in containment flows. During the natural mixing and dilution processes, thermal radiation can affect the fluid temperatures and thereby influence the buoyancy forces in the presence of large amounts of steam. In order to quantify the effect of thermal radiation, an efficient Monte Carlo method with statistical narrow band correlated-k (SNBCK) nongray gas model has been implemented to solve the radiative transfer equation within the framework of *containmentFOAM*. The tailored Monte Carlo solver is validated against the OECD/NEA SETH-2 PANDA ST1 experiments, and it is proven that gas radiation has a significant effect on the gas temperature field and the helium-steam mixing process. The results clearly indicate that gas radiation cannot be neglected in containment flows even at modest temperature differences ($\Delta T < 50K$).

Keywords: Monte Carlo method, nongray gas radiation, *containmentFOAM*, thermal radiation

---

Nomenclature

ϵ	emissivity
η	wavenumber (cm^{-1})
κ_η	absorption coefficient (m^{-1})
$\nabla \cdot q_r$	radiative source term ($W\,m^{-3}$)

---

[*] Correspondence: s.kelm@fz-juelich.de; Tel.: +49 2461 613871

Preprint submitted to Journal of LaTeX Templates *July 20, 2022*

ν_t	turbulent kinematic viscosity ($kg\,m^{-1}\,s^{-1}$)
Ω	solid angle (sr)
ω	turbulence dissipation rate (s^{-1})
ρ	density ($kg\,m^{-3}$)
τ	turbulent shear stress ($kg\,m^{-1}\,s^{-2}$)
ξ	pseudo random number
D	molecular diffusion coefficient ($m\,s^{-2}$)
g	cumulative function
g	gravitational acceleration ($m\,s^{-2}$)
h_i	$i-th$ specie total enthalpy ($kg\,m^2\,s^{-2}$)
h_{tot}	total enthalpy ($kg\,m^2\,s^{-2}$)
I_η	radiative intensity ($Wm^{-2}\,sr^{-1}\,cm^{-1}$)
$I_{b,\eta}$	emission radiative intensity ($Wm^{-2}\,sr^{-1}\,cm^{-1}$)
k	turbulent kinetic energy ($m^2\,s^{-2}$)
p	pressure ($kg\,m^{-1}\,s^{-2}$)
Pr_t	turbulent Prandtl number
q_r	radiative wall heat flux ($W\,m^{-2}$)
r	position vector (m)
Sc_t	turbulent Schmidt number
U	velocity vector ($m\,s^{-1}$)
Y_i	$i-th$ specie mass fraction
n	surface normal vector

1. Introduction

During a postulated severe nuclear accident, large quantities of steam, hydrogen, and radioactive fission products are released from the reactor coolant loop into the containment building. Heat transfer between the containment atmosphere and structures determines its pressurization as well as the hydrogen transport and mixing processes. The local accumulation of hydrogen in the containment building and a subsequent combustion or detonation might occur and challenge the integrity of containment building, internal structures and systems. To support the design and assessment of safety systems (e.g. passive auto-catalytic recombiners or ignitors) or operator actions (e.g., spray or containment cooler activation) a detailed understanding of hydrogen transport in the containment during a severe accident is crucial. In the past, the impact of gas radiation heat transfer was neglected in the CFD analysis of hydrogen mixing due to modest temperature levels ($\leq 800\,K$) prevailing in the containment atmosphere. However, during a loss-of-coolant accident (LOCA) the steam volume fraction can be larger than 60% molar fractions (Sehgal, 2011). Steam has a high absorption effect in the infrared spectrum (Modest, 2013), and the gas radiation heat transfer is important for the hydrogen-steam-air mixing process in containment studies. Although the thermal radiation is not the dominant heat transfer mode in containment flows, it competes with conduction and convection over a long time ($\sim$ *hours*) in the buoyancy driven flows (Soucasse et al., 2012). Consequently, thermal radiation heat transfer inside the containment atmosphere needs to be considered for an accurate prediction of the hydrogen transport and distribution. Furthermore, the gas temperature determines the saturation pressure of water and it influences the steam content in gas phase, containment pressurization and hydrogen flammability in containment flows.

Recently, it has been found that the thermal radiation heat transport plays a significant role for low velocity flows in the large scale facilities like THAI (Gupta et al., 2015; Kumar et al., 2020) (Becker Technologies, Germany) and PANDA (Paladino et al., 2013; Dehbi et al., 2019) (PSI, Switzerland). Cheng et al. (2000) calculated the contribution of surface-to-surface radiation towards the passive decay heat removal system in containment safety analysis, whereas Dehbi et al. (2019) investigated the effect of surface-to-surface radiation on natural convection flows for the DIANA cavity and the THAI TH24 experiment. Both analysis indicate that the radiative source term, which is proportional to the fourth power of the temperature, is comparable to the convection and conduction in natural convection flows. Even more, the mixing process, predicted considering gas radiation was significantly more consistent with the experimental data than the simulation results without using a radiation model.

Under LOCA conditions the surface-to-surface radiation alone is not sufficient in containment safety analyses. The gas radiation heat transport is crucial to predict the temperature distribution with high accuracy in containment studies. Since the radiative properties of steam vary strongly across the spectrum (Modest, 2013), solving thermal radiative transport with nongray gas media is a challenging task in a high-dimensional space consisting of position, radiation direction and wavelength. For this reason, a tailored Monte Carlo solver with the SNBCK nongray gas model is developed based on the *containmentFOAM* (Kelm et al., 2021) framework to solve the radiative heat transfer equation. It is validated against three different OECD/NEA SETH-2 PANDA test cases, ST1_1_2, ST1_2, and ST1_3, characterized by a variation of the injection rate, i.e. convective contribution, illustrating the effect of gas radiation heat transfer in steam mixtures.

2. Modeling approach

2.1. CFD and radiative transfer equation

Generally, containment flows are of multi-component, multi-phase and multi-physics in nature. The application of the CFD method as a tool to predict hydrogen transport and gas mixing processes in the reactor containment is continuously increased in the past few decades. Moreover, the open source CFD

package OpenFOAM (www.openfoam.com and www.openfoam.org)is applied to solve multi-physics issues in the nuclear community by using high performance computing techniques (Fiorina et al., 2022). Based on the advanced CFD algorithms and libraries in OpenFOAM-v6, the *containmentFOAM* solver is developed at the Forschungszentrum Jülich for the containment safety assessment related to containment pressurization, hydrogen mixing process, condensation and passive safety system (Kelm et al., 2021, 2019; Kampili et al., 2021). The governing equations are shown below.
Continuity equation

$$\frac{\partial \rho}{\partial t} + \nabla \cdot (\rho U) = 0 \tag{1}$$

Momentum conservation

$$\frac{\partial (\rho U)}{\partial t} + \nabla \cdot (\rho U U) = -\nabla p + \nabla \cdot \tau + \rho g \tag{2}$$

Species transport equation

$$\frac{\partial (\rho Y_i)}{\partial t} + \nabla \cdot (\rho U Y_i) = -\nabla \cdot \left[\rho \left(D + \frac{\nu_t}{Sc_t} \right) \nabla Y_i \right] \tag{3}$$

Total enthalpy (h_{tot}) transport equation is

$$\begin{aligned} \frac{\partial (\rho h_{tot})}{\partial t} \quad &+ \quad \nabla \cdot (\rho U h_{tot}) = \rho U \cdot g + \frac{\partial p}{\partial t} + \nabla \cdot \left[\left(\lambda + \frac{\rho c_p \nu_t}{Pr_t} \right) \nabla T \right] \\ &+ \sum_{i=1}^{n} \nabla \cdot \left[\rho h_i \left(D + \frac{\nu_t}{Sc_t} \right) \nabla Y_i \right] - \nabla \cdot q_r \end{aligned} \tag{4}$$

The mixture density is computed according to the ideal gas equation

$$p = \rho R T \tag{5}$$

where U is the velocity vector; ρ is the density; p is the pressure; τ is the Reynolds stress; g is the gravitational acceleration; Y_i is the i-th specie mass fraction; D is the molecular diffusion coefficient; ν_t is the kinematic viscosity; Sc_t is the turbulent Schmidt number; λ is the thermal conductivity; h_{tot} is the total enthalpy; h_i is the i-th specie enthalpy.
The buoyancy turbulence model (Kampili et al., 2021) in *containmentFoam* is the $k - \omega$ SST model to calculate the turbulent viscosity ν_t.

$$\frac{\partial (\rho k)}{\partial t} + \nabla \cdot (\rho U k) = P - \beta^* \omega k + \nabla \cdot [(\mu + \sigma_k \mu_t) \nabla k] + P_{k,b} \tag{6}$$

$$\frac{\partial (\rho \omega)}{\partial t} + \nabla \cdot (\rho U \omega) = \frac{\gamma}{\nu_t} P - \beta \rho \omega^2 + \nabla \cdot [(\mu + \sigma_\omega \mu_t) \nabla \omega] + 2(1 - F_1) \frac{\rho \sigma_{\omega 2}}{\omega} \nabla k \cdot \nabla \omega + P_{\omega,b} \tag{7}$$

where k is turbulent kinetic energy; P is turbulence production; ω is turbulence dissipation rate; $P_{k,b}$ is turbulence production due to buoyancy; ν_t is turbulent kinematic viscosity; $P_{\omega,b}$ is turbulence dissipation due to buoyancy; F_1, F_2 are blending functions; $\beta^*, \sigma_k, \beta, \gamma, \sigma_\omega, \sigma_{\omega 2}, \gamma_1, C_3, a_1$ are model constants. The model constants and the blending functions are computed according to standard $k - \omega\ SST^1$ model.

The algorithm details about the *containmentFoam* solver are described in Kelm et al. (2021) and Kampili et al. (2021), while this paper mainly focuses on the modeling and implementation of thermal radiation. Given the temperature, total pressure, and partial pressure from the CFD solver, the radiation heat transfer contribution is modeled as a radiative source term ($\nabla \cdot q_r$) in the energy equation. In buoyancy flows or low velocity flows with high steam concentration, the radiative source term can affect the temperature field significantly, thereby changing the local gas densities and hence the fluid flow. Before introducing the Monte Carlo method, the radiative transfer equation is shortly discussed. The spectral radiative transfer equation (Modest, 2013) (RTE) within a non-scattering medium is shown in Eq. (8).

$$\Omega \cdot \nabla I_\eta(r, \Omega) = -\kappa_\eta I_\eta(r, \Omega) + \kappa_\eta I_{b,\eta}(r, \Omega) \tag{8}$$

where η is the wavenumber; κ_η is the spectral absorption coefficient; I_η is the spectral intensity; $I_{b,\eta}$ is the emission spectral intensity; r is the position vector; Ω is the solid angle. The radiation outcoming intensity $I_\eta(r_{wall}, \Omega)$ at an opaque wall is given by

$$I_\eta(r_{wall}, \Omega) = \epsilon I_{b,\eta}(r_{wall}, \Omega) + \frac{1-\epsilon}{\pi} \int_{n \cdot \Omega' < 0} I_\eta(r_{wall}, \Omega') \left| n \cdot \Omega' \right| d\Omega' \tag{9}$$

where ϵ is the surface emissivity; $\Omega^{'}$ is the incoming direction on the boundary surface; n is the surface normal direction. The outcoming intensity $I_\eta(r_{wall}, \Omega)$ on the boundary surface has two contributions: surface emission and reflection. The first term on the right hand side of Eq. (9) corresponds to the emitted spectral radiative intensity from the wall and the second term accounts for the reflection of all incoming spectral radiative intensities. Theoretically, the RTE boundary condition at opaque walls is neither a Dirichlet condition nor Neumann condition, but a mixed boundary condition if the wall emissivity is not equal to one.

Once the radiation intensity $I_\eta(r, \Omega)$ is solved, the radiative source term $\nabla \cdot q_r$ is equal to the difference between absorbed and emitted radiative energy

$$\nabla \cdot q_r = \int_\eta \int_{4\pi} \kappa_\eta I_{b,\eta}(r, \Omega) d\eta d\Omega - \int_\eta \int_{4\pi} \kappa_\eta I_\eta(r, \Omega) d\eta d\Omega \tag{10}$$

The first term on the right hands side is the black body emission, and the second

---

[1] SST-2003, according to https://turbmodels.larc.nasa.gov/sst.html

term is the radiative absorption. Similarly, the radiative wall heat flux q_r is the difference between incoming radiative heat flux and outgoing heat flux

$$q_r = \epsilon \int_0^\infty \int_{\Omega' \cdot n < 0} I_\eta(r_w, \Omega') |\Omega' \cdot n| d\Omega' d\eta - \epsilon \int_0^\infty \pi I_{b,\eta}(r_w, \Omega) d\eta \tag{11}$$

where n is the boundary surface normal vector.

2.2. Statistical narrow band correlated-k model

Radiative properties of real gases (e.g., H_2O and CO_2) have a highly irregular dependence on the wavenumber ($\eta = 1/\lambda$). Consequently, the modeling of radiative heat exchange in participating infrared active gases is a complex issue. The steam absorption coefficient is not only dependent on the temperature and pressure, but also its molar fraction (Riviere and Soufiani, 2012). The line-by-line model (LBL) is the most accurate nongray gas model and the cornerstone of other simplified nongray gas models, as it is based on the quantum theory of molecules (Goody and Yung, 1995). The main drawback of the LBL model is the computational effort with the consideration of all transition lines in the IR spectrum (e.g., H_2O has more than 100 million transition lines in the HITEMP database (Rothman et al., 2010)). Considering the balance between cost and accuracy, a new tailored SNBCK database for H_2O is generated to couple with the Monte Carlo thermal radiation solver. The detailed discussion about the SNBCK method has been given by Goody and Yung (1995), Riviere and Soufiani (2012) and Modest (2013). In the SNBCK model, the whole spectrum is divided in to a number of small bands (25 cm^{-1}), and the spectral black body emission intensity remains constant in such narrow bands. The averaged narrow band transmissivity for a homogeneous temperature, pressure, and molar fraction media is only an integral function of absorption coefficient κ_η and path length L. The correlated-k method utilizes the reordering technique to calculate the ~~total~~ transmissivity, by converting the wavenumber integration into the absorption coefficient integration using the Jacobian transformation, see Eq. (12).

$$\tau_{\Delta\eta} = \frac{1}{\Delta\eta} \int_{\Delta\eta} e^{-\kappa_\eta L} d\eta = \int_{\kappa_{min}}^{\kappa_{max}} e^{-\kappa_\eta L} \left| \frac{d\eta}{d\kappa_\eta} \right| d\kappa_\eta \tag{12}$$

where $\tau_{\Delta\eta}$ is the average transmissivity; $\Delta\eta$ is the spectral band width; κ_{min} and κ_{max} are the minimum and maximum absorption coefficients; L is the path length.

In computational mathematics, there are many ways to approximate the integral formula, and the Gauss quadrature is an efficient method to approximate the integration

$$\tau_{\Delta\eta} = \int_{\kappa_{min}}^{\kappa_{max}} e^{-\kappa_\eta L} \left| \frac{d\eta}{d\kappa_\eta} \right| d\kappa_\eta \approx \sum_{q=1}^{N_q} w_q e^{-\kappa_q L} \tag{13}$$

where N_q is the quadrature number; κ_q and ω_q are the absorption coefficient and the quadrature weight. Normally, 7-points Gauss quadrature set is sufficient to give an accuracy approximation ($< 2\%$). It is worth noting that the 7-points κ_q and ω_q parameters are given for each narrow band in the SNBCK model.

A new tailored steam SNBCK-FZJ database is generated from the HITRAN2016 (Gordon et al., 2017) database for a list of temperature points from 300 to 1000 K and the steam molar fractions at 0.01, 0.1, 0.2, 0.4, 0.6, 0.8 and 1.0. The spectrum range for the SNBCK-FZJ database is from 50 to 8000 cm^{-1} with 159 narrow bands. It has 7 Gauss points (κ_q^{band}, ω_q^{band}) in each narrow band ($q = 1 - 7$ and $band = 1 - 159$). Therefore, totally 1113 spectral bands are provided to represent the steam gas property in the whole infrared spectrum. The new SNBCK-FZJ parameters have been verified against the HITRAN database in detail. The narrow band transmissivities obtained from LBL and SNBCK-FZJ are compared in Fig. 1. The LBL results are averaged over 25 cm^{-1} in order to compare with the SNBCK-FZJ. The SNBCK-FZJ results are in an excellent agreement with the LBL results. The average deviation of the transmissivity is less than 0.001, and the maximum deviation is about 0.02 in low wavenumber regions. Thus, the SNBCK-FZJ database provides a reliable approximation for the steam nongray gas property.

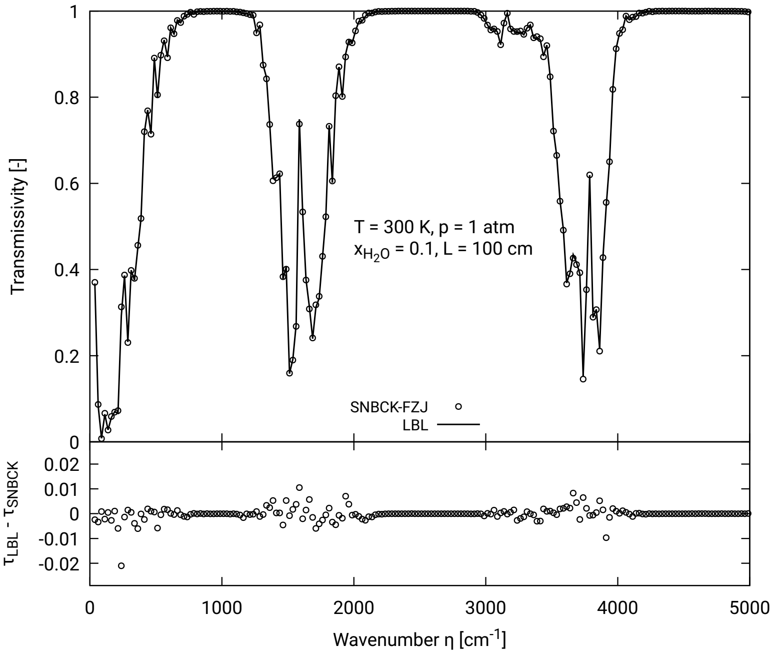

Figure 1: LBL and SNBCK narrow band transmissivity comparison: $T = 300\,K$, p= $1\,bar$, $x_{H_2O} = 0.1$, L = 100 cm

2.3. Monte Carlo method

Thermal radiation can transfer heat over a longer distance than conduction and convection, which can smooth temperature gradients and thereby affect buoyancy forces. However, modeling the radiative heat transfer is a difficult task even using high performance computing owing to the spectral absorption coefficient, the variation of temperature and pressure, and the coupling of the spatial and solid angle discretization. Among RTE solvers, the most widely applied method is the finite volume discrete ordinates method (fvDOM) (Chai et al., 1994). Unfortunately, the computational effort becomes expensive for the fvDOM solver in a fine mesh (millions of cells). The fvDOM solver suffers from false scattering and ray effect, which may become significant in large complex 3D geometries, , e.g. containment buildings (Chai et al., 1993; Chen, 2005). Therefore, a new thermal radiation Monte Carlo solver is developed for containment studies.

The Monte Carlo method is a stochastic process modeling based on a pseudo random number generator, which is one of the optimal algorithms for many computational fields, e.g. neutron reactions (Spanier and Gelbard, 2008). The radiation Monte Carlo solver, at first, generates a large number of energy bundles/photons with different positions, directions and wavenumbers according to the probability density functions. After that, those representative energy bundles/photons interact with the participating media based on the Lambert-Beer law (Howell et al., 2010; Fuwa and Valle, 1963). According to the Lambert-Beer law, the radiation intensity I_η decreases exponentially with the path length s within the absorbing medium

$$I_\eta(s) = I_\eta(0)\exp(-\kappa_\eta s) \tag{14}$$

where κ_η is the spectral absorption coefficient; $I_\eta\,(s)$ is the outcoming radiation intensity; s is the traveling distance; $I_\eta\,(0)$ is the incoming radiation intensity.

The Lagrangian photon tracking process is continued until the energy of photon is low enough to quit. It is noted that the thermal radiation solver uses the same mesh as the CFD simulation. Finally the radiative source term or wall heat flux is estimated by the difference between absorbed and emitted energy (see Eq. (10) and Eq (11)). The total black body emission of the cell i is only determined from the local temperature, pressure, and specie components. However, the total absorbed energy is related to the temperature and absorption coefficient distributions and boundary conditions. For the boundary surface A_j (temperature T_j and area S_j) with gray gas emissivity ϵ, the total emission is

$$Qe_j = S_j \int_0^\infty \epsilon\,\pi I_{b,\eta}(T_j,\,\Omega)\,d\eta \tag{15}$$

For the control volume with nongray gas media, the total emission is quite different from the boundary surface emission owing to the complex interaction between infrared photons and gas molecules. The spectral absorption coefficient is a function of temperature T, pressure p, and mass fraction Y. The total emission from the cell i with the emitting nongray gas is shown in Eq. (16)

$$Qe_i = V_i \int_\eta \int_{4\pi} \kappa_\eta(T_i,\,p,\,Y) I_{b,\eta}(T_i,\,\Omega) d\eta d\Omega \tag{16}$$

where T_i is the cell temperature; κ_η is the spectral absorption coefficient; $I_{b,\eta}$ is the black body emission intensity and V_i is the cell volume.
Therefore, the radiative wall heat flux at surface j is

$$q_{wall}^{j} = \frac{1}{A_j}\left[\sum_{k=1}^{N_{cell}+N_{face}} Qe_k \mathcal{F}_{k\rightarrow j} - Qe_j\right] \tag{17}$$

and the radiative source term (Tessé et al., 2004) at cell i is

$$\nabla \cdot q_r^i = \frac{1}{V_i}\left[Qe_i - \sum_{k=1}^{N_{cell}+N_{face}} Qe_k \mathcal{F}_{k\rightarrow i}\right] \tag{18}$$

where $\mathcal{F}_{k\rightarrow j}$ is the view factor, which describes the proportion of emitted energy from the emitted element (cell or surface) k projected into the surface j; $\mathcal{F}_{k\rightarrow i}$ is the view factor, which describes the proportion of emitted energy from the emitted element (cell or surface) k projected into the cell i. As shown in Eq. (15) and Eq. (16), it is not hard to calculate the radiative emission term. The most challenging part of the thermal radiation is the spectral absorption coefficient κ_η and the view factor $\mathcal{F}$.

The Monte Carlo method can handle the highly angular and spatial radiation intensity, the spectral dependency of absorption coefficient, the fog/soot scattering effect, and the transparent boundary surface without a significant increase in the computation effort. The probability distribution function for the emission position (x, y, z) at the control volume is given by

$$f(x, y, z) = \frac{1}{\Delta V} \tag{19}$$

For the emission direction $\Omega(\theta, \phi)$, the radiative direction emitted from cell i is uniform distribution among solid angle.

$$f(\phi) = \frac{1}{2\pi},\ 0 \leq \phi \leq 2\pi \tag{20}$$

$$f(\theta) = \frac{sin\theta}{2},\ 0 \leq \theta \leq \frac{\pi}{2} \tag{21}$$

As stated before, the SNBCK model is applied to take into account of nongray gas properties in the Monte Carlo solver. The first step is to determine the emission band b for the sampling bundle. The variable of emission band b follows the discrete probability distribution, and the probability $P(b)$ for the emission band b is given in Eq. (22). As shown in Eq. (22), there are 7 quadrature points for each band in the SNBCK model, and the total band number is 159

(N_b =159) over the whole spectrum.

$$P(b) = \frac{\sum_{q=1}^{N_q} \omega_q \kappa_{b,q} I_{b,\eta}(T, \eta_b) \Delta\eta_b}{\sum_{b=1}^{N_b} \sum_{q=1}^{N_q} \omega_q \kappa_{b,q} I_{b,\eta}(T, \eta_b) \Delta\eta_b} \tag{22}$$

where N_b is the number of narrow bands; ω_q is the associated weight; $\kappa_{b,q}$ is the absorption coefficient; $I_b(T, \eta_b)$ is the black body emission intensity in the band center η_b; $\Delta\eta_b$ is the band width.
After that, the quadrature point q is sampled in the narrow band b, and the probability $P(q|b)$ for the quadrature point q is given in Eq. (23).

$$P(q|b) = \frac{\omega_q \kappa_{b,q}}{\sum_{q=1}^{N_q} \omega_q \kappa_{b,q}} \tag{23}$$

During the photon tracking procedure, those two sampling parameters (b, q) are required to determine the absorption coefficient $\kappa_{b,q}$. Obviously, the total emission for the cell i is approximated by

$$Qe_i = 4\pi \sum_{b=1}^{N_b} \sum_{q=1}^{N_q} \omega_q \kappa_{b,q} I_{b,\eta}(T, \eta_b) \Delta\eta_b V_i \tag{24}$$

If the number of sampling bundles for the cell i is $Nrays$, the energy of each bundle is

$$E = \frac{Qe_i}{Nrays} \tag{25}$$

After all the sampling bundles are determined $(x, y, z, \theta, \phi, E, b, q)$, the tracking procedure is based on the physical interaction between photon and media. The energy deposition along its path is calculated according to the Beer-Lambert law. In order to track the bundles efficiently in the computational domain, it is divided into a number of nonoverlapping cells and boundary surfaces using the CFD grid with constant fluid parameters. Each control volume is accurately defined according to several characteristics: boundary faces, surface orientation, volume, cell to cell relations, and face to cell relations. It is convenient to apply same mesh for thermal radiation calculation and CFD solution; however, the Lagrangian particle tracking efficiency is highly related to the number of cells in the CFD grid. There are some Monte Carlo thermal radiation solvers, which apply the coarsening mesh technology for the particle tracking, but the CFD and Monte Carlo remapping scheme is also a challenging issue (Kuczyński and Białecki, 2014).

This photon tracking procedure is explained for the two dimensional grid as shown in Fig. 2. The same principles and algorithms are applied in the three dimensional grid. The computational domain is divided into five cells and it has two sampling energy bundles in each cell. But the number of sampling bundles is not limited to that. If the initial positions, direction, emission energy and wavenumber $(x, y, z, \theta, \phi, E, b, q)$ are determined from the photon sampling algo-

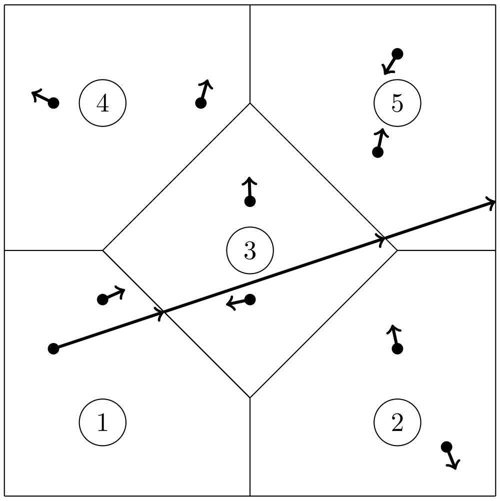

Figure 2: Monte Carlo ray tracking procedure

rithm in the previous section, the next step is to calculate the nearest boundary distance. The cell ① is bounded by five boundary faces, and the distance to each boundary face is calculated. The minimum distance to the nearest can be easily identified (see Fig. 2). Then, the energy deposition within the control volume is related to the current cell absorption coefficient κ. So the bundle emission energy is attenuated along the path length s according to the Beer-Lambert law. It is worthwhile to note that the absorption coefficient κ is the function of (T, p, Y, b, q) in cell ①. The fraction that is absorbed by the medium through the distance s can be defined as the absorbance

$$\alpha = 1 - \exp(-\kappa s) \tag{26}$$

Hence, the energy deposition within cell ① along the path length s is given in Eq. (27), and the array variable Qa is the accumulation of the absorbed energy.

$$Qa[cell\,①]^{new} = Qa[cell\,①]^{old} + E[1 - \exp(-\kappa\, s)] \tag{27}$$

And the residual energy is

$$E^{new} = E^{old} \exp(-\kappa\, s) \tag{28}$$

After passing the boundary face, the particle cell is changed to the neighbour cell ③. The tracking procedure continues unless the particle photon reaches the wall boundary or the energy drops below the cutoff energy. The implemented Monte Carlo method is illustrated in Algorithm 1.

The only limitation of the Monte Carlo method is the statistical error, resulting in a nonphysical temperature fluctuation. In order to obtain reasonable results, a large number of bundles are tracked since the relative error decreases

Algorithm 1: SNBCK Monte Carlo algorithm

```
$cloud = Initialize\_Tracking\_Cloud()$;
for $i = 1$ to $cells$ do
    $Update\_SNBCK\_Absorption\_Coefficient(T,\ p,\ Y)$;
    $Qe[i] = Total\_Emission\_Cell(\kappa,\ T)$ ;
    $Qa[i] = 0$ ;
    for $ray = 1$ to $Nrays$ do
        $x, y, z = Sample\_Point\_within\_Cell()$;
        $u, v, w = Sample\_Direction\_within\_Cell()$;
        $E = Qe[i]/Nrays$ ;
        $b, q = Sample\_Wavenumber\_Cell(\kappa\ ,T)$ ;
        $cloud.addPhoton(x,\ y,\ z,\ u,\ v,\ w,\ E,\ b,\ q)$;
    end
end

for $photon = 1$ to $Nphotons$ in $cloud$ do
    while $photon.E > cutoff$ do
        $ds = Distance\_Next\_Boundary()$;
        $\kappa = SNBCK\_Absorption\_Coefficient(T,\ p,\ Y,\ b,\ q)$ ;
        $\alpha = \exp(-\kappa \cdot ds)$;
        $Qa[Cell] = Qa[Cell] + \alpha \cdot photon.E$ ;
        $photon.E = (1 - \alpha) \cdot photon.E$;
        if photon.onBoundary_Face() then
            $Boundary\_Treatment()$ ;
        end
        $Cell = Change\_Next\_Cell()$ ;
    end
    $cloud.deletePhoton()$;
end

for $i = 1$ to $cells$ do
    $divQr[i] = (Qe[i] - Qa[i])/\Delta V$ ;
end
```

with the square root of the number of photons. Due to the efficiency reason, different optimization methods (e.g., importance sampling (Zhang et al., 2009) and emission-based reciprocity Monte Carlo method (Tessé et al., 2004)) are implemented in the *containmentFOAM* radiation library. The importance sampling technology is a bias sampling method according to the global maximum and minimum temperature obtained from the previous CFD time-step, in which there are more sampling photons in the radiative heat source region than other regions. Therefore, the important sampling method reduces the number of tracked bundles without losing the accuracy, making Monte Carlo applicable to the engineering applications. Recently, the emission-based reciprocity Monte Carlo method was proposed by Tessé et al. (2004) in order to reduce the Monte Carlo statistical error. The emission-based reciprocity Monte Carlo significantly improves the efficiency without increasing the number of photons by assuming that on each photon path, and the bundle can reverse in both directions. In other words, it can virtually double the number of photons for this algorithm. Furthermore, there is no energy exchange between two cells of the same temperature. The emission-based reciprocity Monte Carlo method is more suitable for applications with modest temperature differences, e.g. the containment flows.

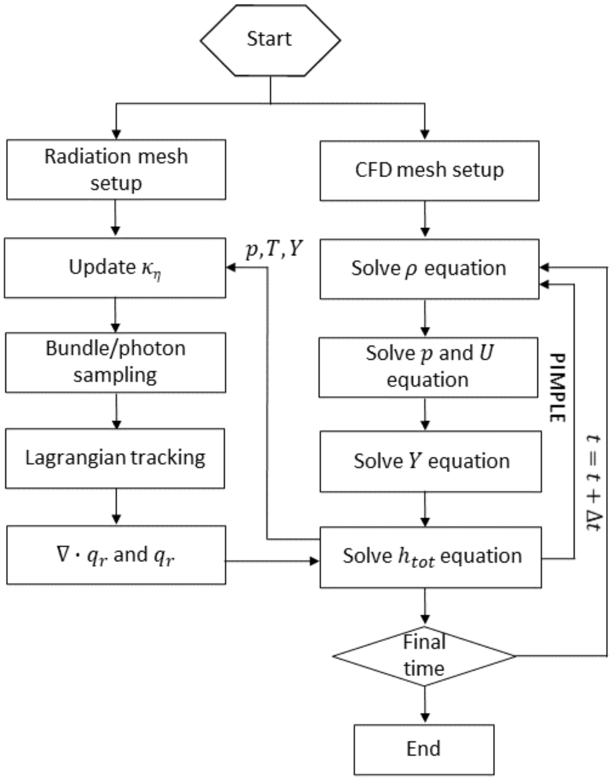

Figure 3: Monte Carlo and CFD coupling algorithm

Thermal radiation is just one heat transfer mechanism in the energy equation, and the accuracy of heat transport modeling is also affected by the turbulence flow. The CFD and thermal radiation coupling algorithm is shown in Fig. 3. When solving the radiative transfer equation, the transient temperature T, total pressure p, and mass fractions Y are mapped to the radiation mesh. The absorption coefficient is updated based on the given temperature and pressure fields, and then the radiative transfer equation is solved. After finishing the radiation calculation, the radiative source term is mapped back the CFD mesh. Since the accurate radiation simulation is computationally more expensive than the CFD modeling, the thermal radiation can only be calculated once for a number of CFD time steps (e.g., every 100th step) and it is simply considered constant during this time period. This approximation is valid for the slowly changing temperature and concentration fields in RANS analysis.

2.4. Verification of the Monte Carlo method

Before integrating the Monte Carlo method into the CFD solver, the algorithm is verified against the analytical 2D test cases by Goutiere et al. (2000). This test case is a two-dimensional rectangular box (1.0 m width, 0.5 m height) discretized with a orthogonal mesh. It is filled with isothermal H_2O-N_2 mixture ($P = 1\,atm$, $T = 1000\,K$, $vol._{H_2O} = 0.2$), and the temperature of black walls are 0 K.

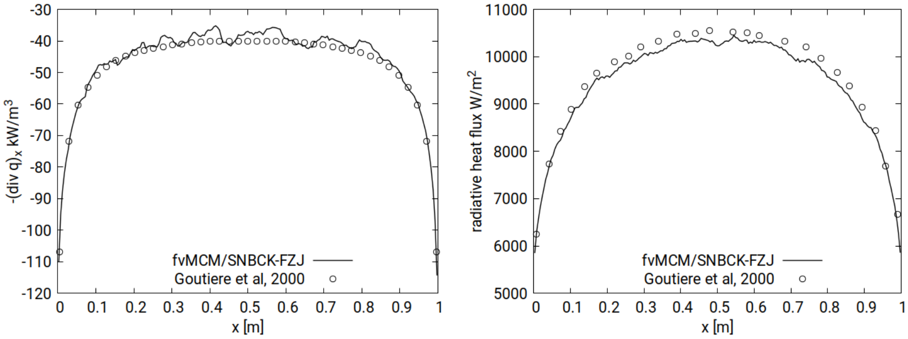

(a) $-\nabla \cdot q_r$ at the centeral line (b) q_r on the bottom wall

Figure 4: Verification of the Monte Carlo algorithm against the Goutiere test case (Goutiere et al., 2000): $T = 1000\,K$, $p_{tot} = 1\,atm$ and $vol._{H_2O} = 0.2$ in the 1.0 m × 0.5 m box

Fig. 4 shows the comparison between the new Monte Carlo method with SNBCK model and the literature reference. There is a numerical fluctuation for Monte Carlo results. But the fvMCM/SNBCK-FZJ result is in a good agreement with the reference. The average relative error is less than 2%, and the maximum relative error is 4% for the radiative wall heat flux. According to this verification case, the SNBCK-FZJ database is reliable for the steam mixtures. The new developed Monte Carlo solver with the SNBCK model can be coupled to the existing CFD solver. The radiative source term is updated outside the PIMPLE loop during the CFD simulations. Due to the low fluid velocity, it is not necessary to perform the radiation calculation at each CFD time step.

3. Validation against PANDA ST1 test series

The PANDA facility is operated at the Paul Scherrer Institute (PSI) Switzerland to investigate the containment thermal-hydraulic phenomena under postulated severe accident conditions. The OECD/NEA SETH-2 PANDA ST1 experiments (Paladino et al., 2013; Andreani et al., 2019) were conducted to study the interaction of low momentum jet with an initially helium-rich layer. There were two main vessels (Vessel 1 and Vessel 2) used in the ST1 experiments, as shown in Fig. 5, and each vessel is 4 m in diameter and 8 m in height with the volume $\sim$ 90 m^3. The vessel 1 and the vessel 2 are connected by a large interconnecting pipe (1 m diameter). In the present work, three ST1 test series with different steam injection velocities (30/60/90 g/s) were considered. For the ST1 test series both vessels were initially filled with 100% $vol.$ steam at 381.13 K under 1.3 atm to avoid bulk condensation. At first, a helium layer with approximate 2 m height was created in the vessel 1. Then, this helium layer was eroded by a vertical hot steam injection (433.15 K) with different flow rates (30/60/90 g/s) from the bottom part of the vessel 1 at the 4 m height (see Fig. 5). The vessel pressure was maintained constant at 1.3 atm through the venting system at the top of the vessel 2. The distance from the injection outlet and the helium layer is about 2 m height. The heat transfer (including thermal radiation) between the hot steam plume and atmosphere can influence the temperature, velocity and density distribution before impinging onto the the bottom of helium layer.

Table 1: PANDA ST1 test experiment parameters

experiments		ST1_1_2	ST1_2_2	ST1_3
Parameters	Units			
initial temperature	K	381	381	381
initial atmosphere		steam	steam	steam
Steam mass flow	g/s	30	60	90
Injection temperature	K	423	423	423
initial pressure	atm	1.3	1.3	1.3
Fr		1.3	2.6	3.8

There are 374 K-type thermocouples inside Vessel 1, Vessel 2 and the innterconnecting pipe for the temperature measurement, and two mass spectrometers were installed for gas concentration measurements. All available temperature and concentration measurements were used for a systematic validation of the model. Considering three different tests (i.e. injection rates), the temperature field around the jet can be used as a measure for the thermal radiation heat transfer and to test the radiation models. Besides that, the erosion transient is investigated by means of the point-wise concentration histories as well as the gas temperature measurements in order to highlight the effect of radiative heat transfer on the mixing process.

In order to describe the transport and mixing processes not just at the layer interface but also in the multi-compartment domain, both vessels are considered in the model geometry. This also allows to avoid the specification of additional boundary conditions or symmetries. The main simplifications are related to the internal structures. Except the straight part of the central injection line, all internal structures and flanges at the bottom part of vessels are neglected. The

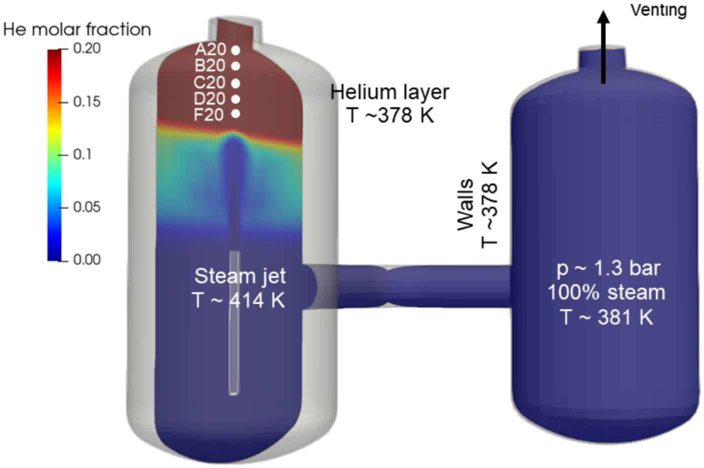

Figure 5: PANDA ST1_1 to ST1_3 test scenario with the central steam injection

fluid domain is discretized by means of a block-structured hexahedral mesh. The steel walls of the vessel are the main heat sink. The boundary walls are resolved in the mesh and a conjugate heat transfer approach is used.

The fundamental modeling strategy follows the baseline model defined in Kelm et al. (2021); Kampili et al. (2021); Kumar et al. (2020). In particular, a URANS approach, closed by the $k-\omega$ STT model (including buoyancy terms) is employed. Initial and boundary conditions are derived from the experimental data sets. In those three tests, the fluid domain is initialized at zero velocity, and the initial helium along the height is defined according to the experiment. The inlet boundary condition is given by the measured transient evolution of the steam mass flow rates ($\sim$30/60/90 g/s) and temperature, while the profiles of U and k at the injection line are mapped from the experiment data. The eddy frequency is estimated by assuming an eddy viscosity ratio of 10.

Gas radiation is modeled using the aforementioned Monte Carlo thermal radiation solver with the SNBCK-FZJ nongray gas model. Between 40 and 80 energy bundles are tracked per cell (in total roughly 800.000 tracking histories) to calculate the radiative source terms in every one second. A number of simulations with different CFD or Monte Carlo settings have been conducted to ensure the independence of parameters (e.g., radiative source term update frequency, number of energy bundles, numerical discretization schemes and solution methods). At all walls a no-slip boundary is defined. The emissivity ϵ of the vessel wall is defined as 0.3 (value measured by PSI for a dry steel sample in the relevant temperature range).

Both vessels are considered in the CFD mesh following the best practice guidelines for CFD in nuclear reactor safety applications (Mahaffy et al., 2007), while the second vessel is meshed rather coarse ($\sim$ 20 % of the nodes) as the flow and transport processes are not considered of significance in this work. The

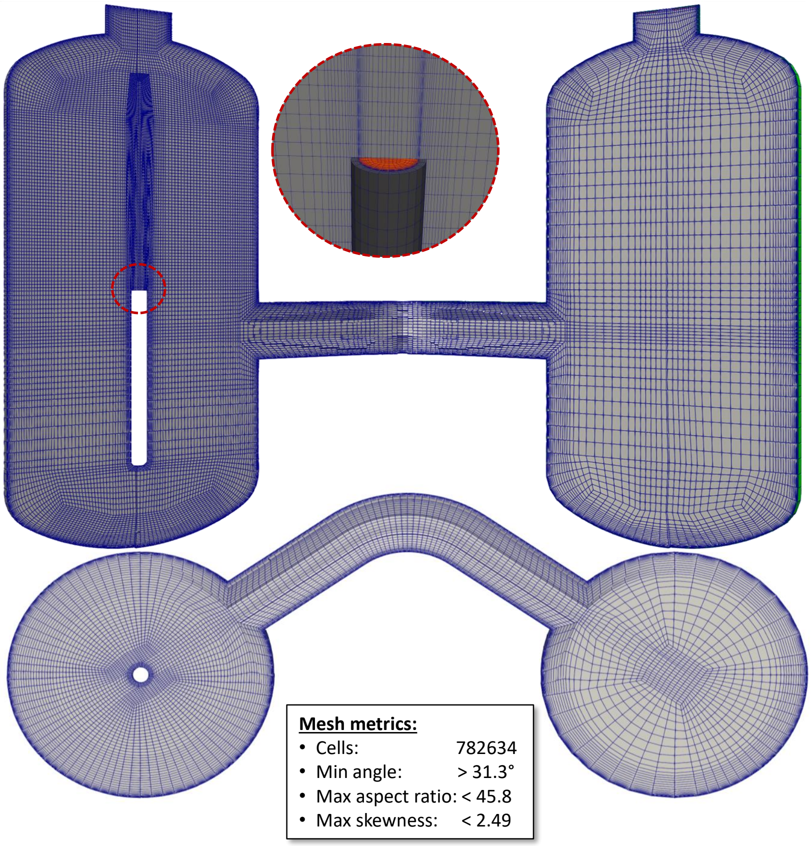

Mesh metrics:
- Cells: 782634
- Min angle: > 31.3°
- Max aspect ratio: < 45.8
- Max skewness: < 2.49

Figure 6: PANDA ST1 CFD mesh

mesh refinements along the injection pipe and near wall regions are required to resolve the free and wall shear stress (see Fig. 6). The mesh quality is optimized in terms of face angle, aspect ratio and volume ratio. The aspect ratio of the cells is small especially above the injection line exit where the significant mixing processes occur where the velocity gradient is large.

Table 2: Mesh sensitivity study for the ST1_3 experiment

Mesh	Number of cells	yPlus (avg.)	Wall heat flux (W)	GCI_U
Coarse	164868	8.92	4113.39	5.61%
Medium	782634	4.57	4227.47	1.05%
Fine	4930096	2.13	4257.84	0.38%

Three different grids are used to perform the mesh sensitivity study for the ST1_3 experiment, which is characterized by the highest Reynolds number and thus the steepest gradients. The thermal radiation is not considered in the mesh sensitivity study for the ST1_3 experiment to reduce the computation effort. The coarse mesh has 164868 hexahedra cells, while there are 4930096 hexahedra cells for the fine mesh (refined by a factor of two in each spatial direction). The mesh sensitivity for three different meshes is summarized in Table 2 at the final equilibrium state ($\sim$ 100 s). In the comparison of the integrated wall heat flux and yPlus values for three difference meshes, there is a numerical error for the coarse mesh. Furthermore, the mesh uncertainty is quantified by the Grid convergence index (GCI) method (Mansour and Laurien, 2018), and the selected vertical velocity point is located at the 7 m height in the vessel 1. The discretization error on the medium mesh is considered to be acceptable and even less for the two other experiments with smaller Reynolds number. Consequently, the medium grid was used for the production runs.

In the following discussion, the best estimate result, the finite volume Monte Carlo method with the SNBCK-FZJ nongray gas model is labeled as 'SNBCK-FZJ'. The impact of gas radiation is again demonstrated by neglecting radiative transport ('No radiation'). The temperature field in the quasi-steady state following the dissolution of the layer is considered as a first measure to evaluate the effect of thermal radiation heat transport. A qualitative comparison of the temperature field surrounding the jet is performed on basis of the 2D temperature contour plots (compare Fig. 7). It is noted that the experimental contours are generated by interpolating between the thermocouple sensors, which in particular leads to an artificially broader illustration of the jet flow. Above the injection elevation (y $\sim$ 4 m), the temperature field is governed by the hot steam jet and the radial radiation heat transfer between the atmosphere.

The gas radiation transfer promotes heat transfer between the hot steam jet and ambient atmosphere, and thus increasing the decay of temperature along the trajectory. The 2D temperature fields from the experiments and simulation with radiation model are consistent; while the simulation without radiation shows a visibly higher gas temperature, which is necessary to allow for a sufficient temperature gradient to the wall for convective heat transfer. Besides turbulent convection in the plume shear layer, the gas radiation can affect the temperature field over a long distance in comparison with the conduction and convection heat transfer mode. In comparison with the 'No radiation' case, the 'SNBCK-FZJ' is in reasonable agreement with the experimental data owing to a stronger heat radiation between the hot jet, atmosphere and walls. Without considering thermal radiation, the temperature distribution at the top of vessel 1 is totally different from the experiment for the ST1_1_2 experiment.

Fig. 8, 9 and 10 compare the simulated and measured temperature profiles along the jet center line for the ST1_1_2, ST1_2_2 and ST1_3, respectively. It is obvious that there is a stronger decay of temperature along the trajectory for the experiment and simulations with gas radiation than for the simulation without radiative heat transfer. On basis of this quasi-steady flow, it is concluded that the gas radiation leads to a homogenization of the temperature field (i.e. less steep temperature gradients between jet, bulk and wall). This effect is evident for high steam concentration with small temperature differences

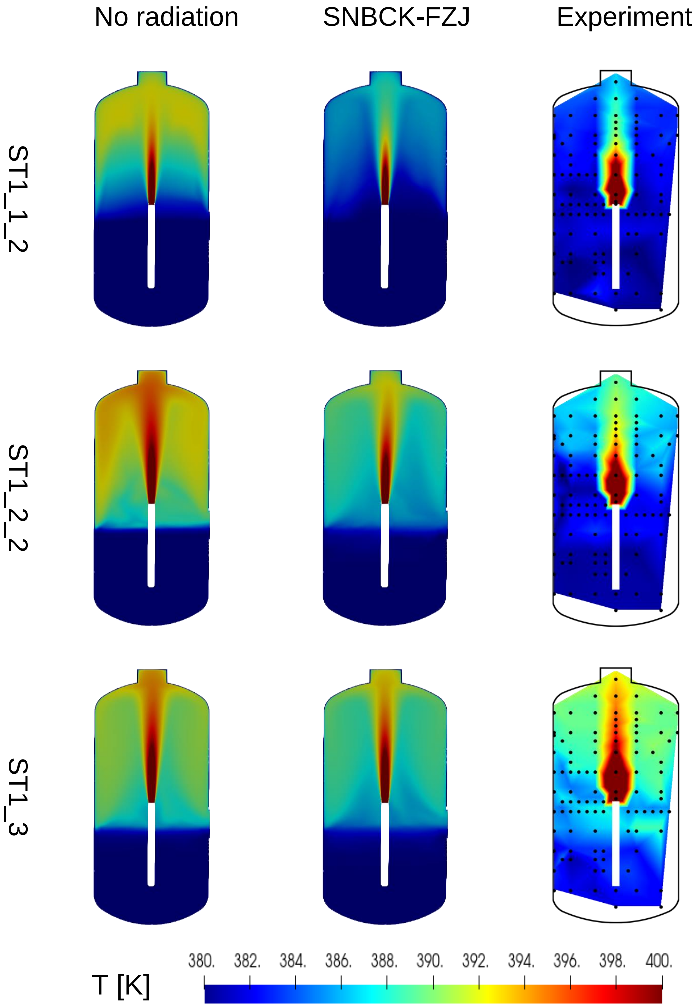

Figure 7: ST1 temperature field at the quasi-steady state

(ΔT jet-ambient < 30 K). This finding is consistent for the three different jet momenta.

Besides the vertical temperature profile, gas radiation also changes the wall heat balance and thus have an effect on wall condensations for two-phase simulations. The comparison of the integrated wall heat fluxes in the quasi-steady state is given in Table 3. The integrated wall heat fluxes for those two settings increase along with the injection velocity ($30/60/90$ g/s). The simulation with thermal radiation for the the ST1_1_2 experiment has a smaller integrated wall

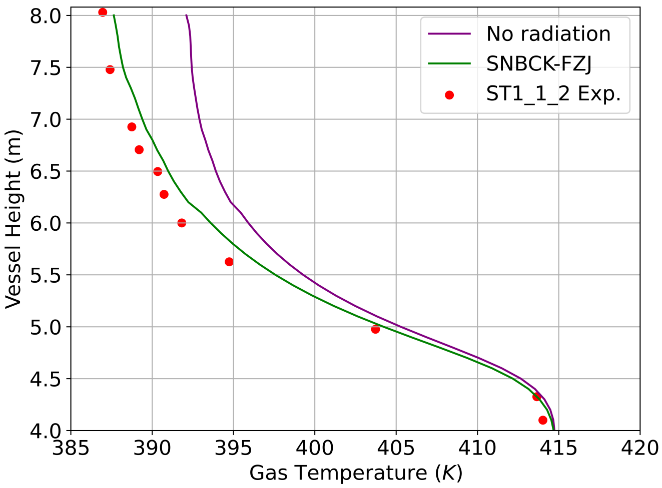

Figure 8: ST1_1_2 central temperature profile at the quasi-steady state

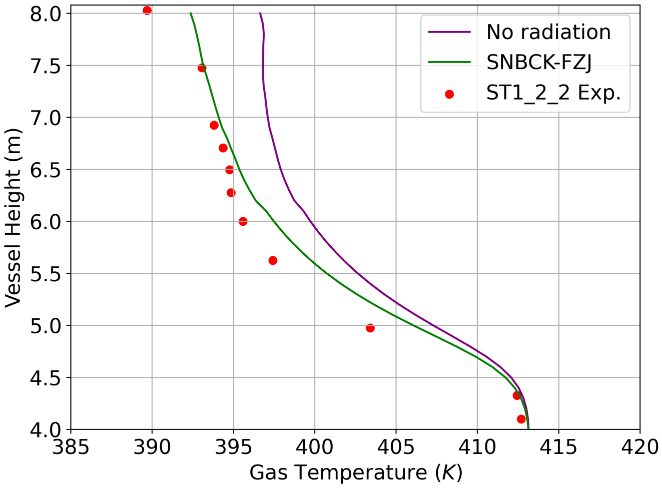

Figure 9: ST1_2_2 central temperature profile at the quasi-steady state

heat flux than that one without radiation consideration, since the convective heat transfer is significantly weakened on the boundary walls (see Fig. 7 and 8). In other two experiments, the total heat transfer (including radiation) between atmosphere and boundary walls becomes stronger than those simulations without radiation, even though the temperature profile is relatively smoother.

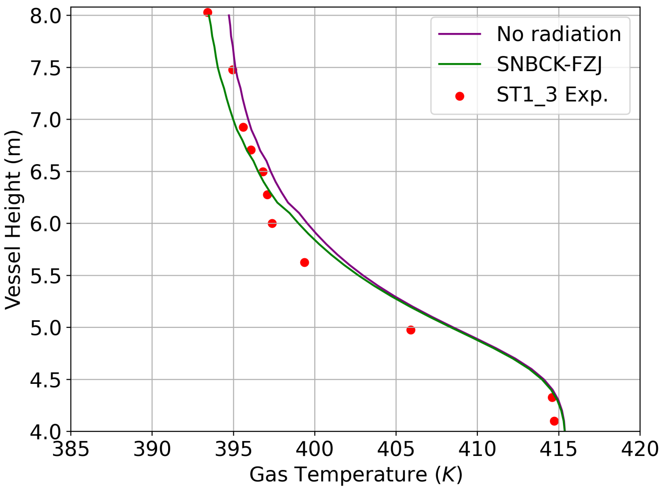

Figure 10: ST1_3 central temperature profile at the quasi-steady state

Table 3: Wall heat fluxes on the boundary wall

Exp.	Model	Convection (W)	Radiation (W)	Integrated (W)
ST1_1_2	No radiation	3955.96	-	3955.96
	SNBCK-FZJ	2240.92	1316.91 (37%)	3557.83
ST1_2_2	No radiation	4781.75	-	4781.75
	SNBCK-FZJ	3624.28	1658.35 (31%)	5282.63
ST1_3	No radiation	4816.49	-	4816.49
	SNBCK-FZJ	4239.71	1546.16 (26%)	5785.87

For the convective heat fluxes, there is a weakening convective heat transfer for both radiation simulations due to temperature profiles. The proportions of radiative wall heat flux in integrated wall heat flux are also given in Table 3. For the ST1_1_2 experiment, the radiative wall heat flux is about 37% of the total wall heat flux. On the basis of the above findings, it is concluded that the gas radiation is crucial for the wall heat balance in containment flows. It can either enhance or diminish the heat transfer between atmosphere and wall depending on the fluid state (e.g. temperature, velocity and specie pressure).

In the ST1_1_2, gas radiation not only influences the temperature distribution, but also changes the mixing process. When increasing the injection velocities, the difference between with radiation and without radiation in the mixing process becomes modest in the ST1_2_2 and ST1_3 experiments. The concentration histories for the uppermost sampling positions for the simulations against the ST1_1_2 helium measurements are shown in Fig. 11, and the positions of concentration sensor can be found in Fig. 7. Without considering thermal radiation, the mixing process is much slower than the 'SNBCK-FZJ'

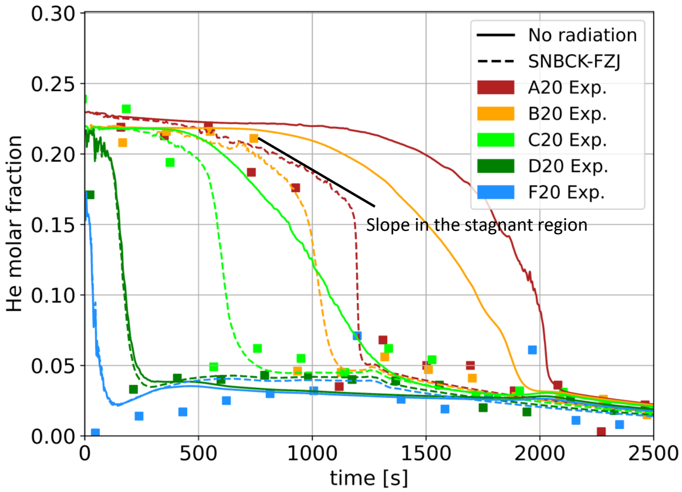

Figure 11: ST1_1_2 transient helium erosion process

case. It is obvious that neglecting thermal radiation leads to a visible retardation of the predicted mixing process compared to the experiment. The slope of the concentration decay in the stagnant layer increases in the 'SNBCK-FZJ' case, while there is only a weak slope due to molecular diffusion for the simulation without radiative heat transfer. This is because the gas radiation transfers heat into the stagnant fluid above the jet stagnation region, where convective transport is hindered by the layer interface. Nevertheless, the increased slope in the concentration history is explained by means of a secondary recirculation inside the stagnant layer, which is driven by small density differences. It is clear that the new developed Monte Carlo model can predict the temperature field as well as the transient helium erosion in consistence with the experiment.

A detailed look at the transient density, velocity and turbulent viscosity fields (e.g. ST1_1_2, see Fig. 12) allows to identify the reason (Only the simulation results are shown, since it is difficult to measure the density field). Because the ST1_1_2 experiment is conducted at constant pressure, the decrease in gas temperature leads to an increase of density. In the early transient (depicted for t=400 s), gas radiation heat transfer changes the density of the gas surrounding the steam jet, but the velocity difference between the 'No radiation' and the 'SNBCK-FZJ' case is negligible in the beginning. The helium mixing process is mainly controlled by the injection momentum and jet entrainment. With increasing mixing, the jet is mainly controlled by the negative buoyancy before and while impinging on the layer interface. This effect is reduced by radiative heat transfer and the 'No radiation' case has a steep density gradient between jet and surrounding gas. This density gradient reduces the jet momentum and in particular affects the flow redirection near the stagnation point. It is clearly

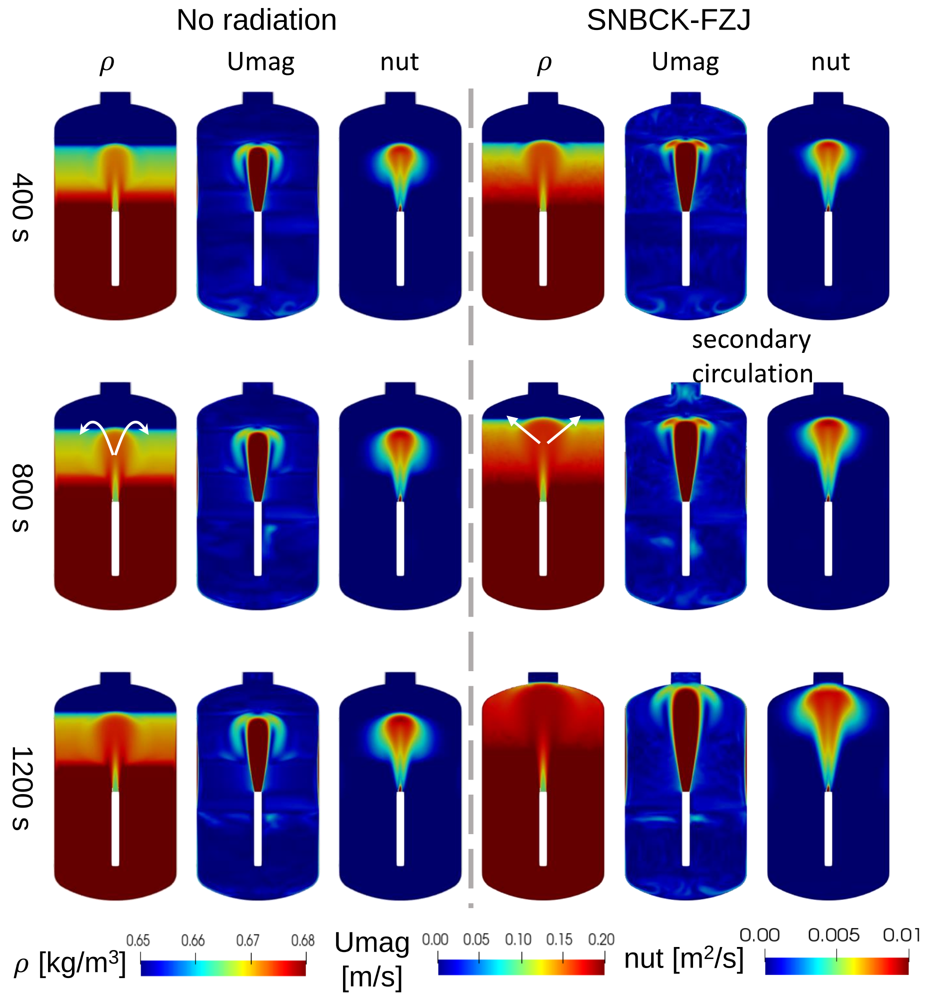

Figure 12: ST1_1_2 density, velocity and turbulent viscosity at different time steps

visible that the gas mixture can spread radially at the interface in the 'SNBCK-FZJ' case, while it is falling down in the 'No radiation' case after loosing its initial momentum (depicted for t=800s). Besides that, thermal radiation has no visible impact on the turbulent viscosity (nut) distribution in the ST1_1_2 experiment. There is an enhancement for the helium mixing process in the horizontal direction for the 'SNBCK-FZJ' case (depicted for t=800s), which is mainly related to the buoyancy balance near the stagnant point of the jet.

Another important finding is the appearance of a weak secondary circulation in the stagnant gas region of the 'SNBCK-FZJ' case. By comparing the velocity field without thermal radiation, it is obvious that thermal radiation mechanism can affect the fluid motion over a certain distance. This internal circulation in the stagnant layer aids the mixing process, which results in a steeper concentration decay, e.g. at the helium sensor A20 (see Fig. 11) and thus a globally faster erosion of the helium layer (compare t=800s and t=1200s) in case radiative heat transport is considered.

It is concluded that the observed helium mixing process is a result of the complex interaction between radiative heat transfer and convective heat and mass transfer in the turbulent buoyancy-affected flow. This implies that a validation case needs to consider this interaction accurately in order to conclude on the validity of individual models such as the turbulence model. Since the CFD and radiation coupling is a nonlinear problem, the accurate thermal radiation solver and nongray gas model can serve as a reference for further model development towards containment analysis.

4. Conclusions

The aim of this paper is to clarify the thermal radiation transfer in nuclear severe accident analysis, which was neglected in low temperature applications ($\leq 800\,K$). If the strength of the thermal radiation is in the order of either conduction or convection, it has a significant effect on the temperature and density fields. For this purpose, a finite volume Monte Carlo solver with the tailored SNBCK nongray gas model is implemented based on the OpenFOAM libraries in the framework of *containmentFoam*. A number of advanced sampling algorithms and optimizations are applied to reduce the the statistical error. Furthermore, three OECD/NEA SETH-2 PANDA ST1 experiments are analyzed to validate the new developed Monte Carlo method. The simulations demonstrate the validity of the the Monte Carlo method and tailored SNBCK model in steam-helium mixtures with relatively low temperatures. Furthermore, integrated in *containmentFOAM*, consistent predictions of the gas temperature fields can be obtained. It is concluded that neglecting radiation in humid gas mixtures results are significantly underpredicted the helium mixing process, especially in the ST1_1_2 experiment. It is emphasized that an accurate thermal radiation solver is mandatory to predict the mixing process over a long time in containment flows, since the interaction between thermal radiation and CFD is a complex issue. In order to quantify the effect of radiative heat transfer in containment flows, further studies with different thermal-hydraulic conditions are required, such as gas temperature difference, steam/CO_2 concentration and gas mixture.

Acknowledgements

The authors gratefully acknowledge the support of all the countries and the international organizations participating in the OECD/NEA SETH-2 project, in particular the members of the Management Board and the Program Review Group. They would also like to thank the PANDA team of Paul Scherrer Institute for preparing, performing and documenting the experiments. We acknowledge the Helmholtz Interdisciplinary Doctoral Training in Energy and Climate

Research (HITEC) for supporting the present work, and the Chinese Scholarship Council (CSC) for the funding of the PhD position

References

Andreani, M., Gaikwad, A.J., Ganju, S., Gera, B., Grigoryev, S., Herranz, L.E., Huhtanen, R., Kale, V., Kanaev, A., Kapulla, R., Kelm, S., Kim, J., Nishimura, T., Paladino, D., Paranjape, S., Schramm, B., Sharabi, M., Shen, F., Wei, B., Yan, D., Zhang, R., 2019. Synthesis of a cfd benchmark exercise based on a test in the panda facility addressing the stratification erosion by a vertical jet in presence of a flow obstruction. Nuclear Engineering and Design 354, 110177. Special Issue on TRENDS AND PERSPECTIVES IN NUCLEAR THERMAL-HYDRAULICS.

Chai, J.C., Lee, H.S., Patankar, S.V., 1993. Ray effect and false scattering in the discrete ordinates method. Numerical Heat Transfer, Part B Fundamentals 24, 373–389.

Chai, J.C., Lee, H.S., Patankar, S.V., 1994. Finite volume method for radiation heat transfer. Journal of thermophysics and heat transfer 8, 419–425.

Chen, Y., 2005. Coupled Monte Carlo-discrete ordinates computational scheme for three-dimensional shielding calculations of large and complex nuclear facilities. Technical Report. Forschungszentrum Karlsruhe GmbH Technik und Umwelt (Germany).

Cheng, X., Erbacher, F., Neitzel, H., 2000. Passive containment cooling by natural air convection and thermal radiation after severe accidents. Nuclear Engineering and Design 202, 219 – 229.

Dehbi, A., Kelm, S., Kalilainen, J., Mueller, H., 2019. The influence of thermal radiation on the free convection inside enclosures. Nuclear Engineering and Design 341, 176–185.

Fiorina, C., Clifford, I., Kelm, S., Lorenzi, S., 2022. On the development of multi-physics tools for nuclear reactor analysis based on openfoam®: state of the art, lessons learned and perspectives. Nuclear Engineering and Design 387, 111604.

Fuwa, K., Valle, B., 1963. The physical basis of analytical atomic absorption spectrometry. the pertinence of the beer-lambert law. Analytical Chemistry 35, 942–946.

Goody, R.M., Yung, Y.L., 1995. Atmospheric radiation: theoretical basis. Oxford university press.

Gordon, I.E., Rothman, L.S., Hill, C., Kochanov, R.V., Tan, Y., Bernath, P.F., Birk, M., Boudon, V., Campargue, A., Chance, K., et al., 2017. The hitran2016 molecular spectroscopic database. Journal of Quantitative Spectroscopy and Radiative Transfer 203, 3–69.

Goutiere, V., Liu, F., Charette, A., 2000. An assessment of real-gas modelling in 2d enclosures. Journal of Quantitative Spectroscopy and Radiative Transfer 64, 299 – 326.

Gupta, S., Schmidt, E., Von Laufenberg, B., Freitag, M., Poss, G., Funke, F., Weber, G., 2015. Thai test facility for experimental research on hydrogen and fission product behaviour in light water reactor containments. Nuclear Engineering and Design 294, 183–201.

Howell, J.R., Menguc, M.P., Siegel, R., 2010. Thermal radiation heat transfer. CRC press.

Kampili, M., Kumar, G.V., Kelm, S., Prakash, K.A., Allelein, H.J., 2021. Cfd simulations of stratified layer erosion in minipanda facility using the tailored cfd solver containmentfoam. International Journal of Heat and Mass Transfer 178, 121568.

Kelm, S., Kampili, M., Kumar, G.V., et al., 2019. Development and first validation of the tailored cfd solver containmentfoam for analysis of containment atmosphere mixing, in: 18th International Topical Meeting on Nuclear Reactor Thermal Hydraulics 2019 (NURETH 2019), American Nuclear Society.

Kelm, S., Kampili, M., Liu, X., George, A., Schumacher, D., Druska, C., Struth, S., Kuhr, A., Ramacher, L., Allelein, H.J., Prakash, K.A., Kumar, G.V., Cammiade, L.M.F., Ji, R., 2021. The tailored cfd package 'containmentfoam' for analysis of containment atmosphere mixing, h2/co mitigation and aerosol transport. Fluids 6.

Kuczyński, P., Białecki, R., 2014. Radiation heat transfer model using monte carlo ray tracing method on hierarchical ortho-cartesian meshes and non-uniform rational basis spline surfaces for description of boundaries. Archives of Thermodynamics 35.

Kumar, G.V., Kampili, M., Kelm, S., Prakash, K.A., Allelein, H.J., 2020. Cfd modelling of buoyancy driven flows in enclosures with relevance to nuclear reactor safety. Nuclear Engineering and Design 365, 110682.

Mahaffy, J., Chung, B., Song, C., Dubois, F., Graffard, E., Ducros, F., Heitsch, M., Scheuerer, M., Henriksson, M., Komen, E., et al., 2007. Best practice guidelines for the use of CFD in nuclear reactor safety applications. Technical Report. Organisation for Economic Co-Operation and Development.

Mansour, A., Laurien, E., 2018. Numerical error analysis for three-dimensional cfd simulations in the two-room model containment thai+: Grid convergence index, wall treatment error and scalability tests. Nuclear Engineering and Design 326, 220–233.

Modest, M.F., 2013. Radiative heat transfer. Academic press.

Paladino, D., Mignot, G., Kapulla, R., Zboray, R., Andreani, M., Tkatschenko, I., Studer, E., Brinster, J., 2013. Oecd/seth-2 project: Panda and mistra experiments addressing key safety issues for water reactor containment, in: The 15th International Topical Meeting on Nuclear Reactor Thermal-Hydraulics, NURETH-15 Pisa, Italy.

Riviere, P., Soufiani, A., 2012. Updated band model parameters for h2o, co2, ch4 and co radiation at high temperature. International Journal of Heat and Mass Transfer 55, 3349–3358.

Rothman, L.S., Gordon, I., Barber, R., Dothe, H., Gamache, R.R., Goldman, A., Perevalov, V., Tashkun, S., Tennyson, J., 2010. Hitemp, the high-temperature molecular spectroscopic database. Journal of Quantitative Spectroscopy and Radiative Transfer 111, 2139–2150.

Sehgal, B.R., 2011. Nuclear safety in light water reactors: severe accident phenomenology. Academic Press.

Soucasse, L., Rivière, P., Xin, S., Le Quéré, P., Soufiani, A., 2012. Numerical study of coupled molecular gas radiation and natural convection in a differentially heated cubical cavity. Computational Thermal Sciences: An International Journal 4.

Spanier, J., Gelbard, E.M., 2008. Monte Carlo principles and neutron transport problems. Courier Corporation.

Tessé, L., Dupoirieux, F., Taine, J., 2004. Monte carlo modeling of radiative transfer in a turbulent sooty flame. International journal of heat and mass transfer 47, 555–572.

Zhang, J., Gicquel, O., Veynante, D., Taine, J., 2009. Monte carlo method of radiative transfer applied to a turbulent flame modeling with les. Comptes Rendus Mécanique 337, 539–549.